The P- and S-Wave Decomposition in a Multicomponent Elastic Wavefield Based on the Divergence and Curl Operators and Their Applications in Elastic Reverse Time Migration

Na Fan, Xiao-Bi Xie, Lian-Feng Zhao, Xiyan Zhou, and Zhen-Xing Yao

***Abstract*— The P- and S-wave separation is an important step in the elastic reverse-time migration (ERTM). It not only removes crosstalk artifacts in the image but also provides additional constrains to subsurface structures by providing images between different wave types. Traditional Helmholtz decomposition based on divergence and curl operations can separate the P and S wave modes but also modify the amplitude, phase and physical dimension of the original coupled wavefields. To recover the separated P- and S-waves to their original forms, we propose a method, in which the corrections to the distorted separated wavefields, including their phase, amplitude and vector polarizations, are organized into two spatial-time domain partial differential equations. Solving these equations can generate the separated P and S wavefields. The method can be conveniently applied in the time-space domain and consistent with most time-domain finite-difference (FD) based ERTM method. To verify the quality of the decomposed P- and S-wave components, we apply them to the ERTM using different elastic image conditions. For the PP image, we use the scalar imaging condition by crosscorrelating the corrected scalar Helmholtz potential wavefield from both source- and receiver-sides. For the PS image, we use the magnitude- and sign-based vector imaging condition by crosscorrelating the magnitudes of the source-side vector P wave and the receiver-side vector S wave, whereas the sign is determined through their dot-product results. Thus, accurate PP- and PS-reflectivity images can be obtained. Several numerical examples are used to verify our elastic wavefield separation method and the ERTM workflow.**

***Index Terms*— Elastic reverse time migration (ERTM), elastic-wave decomposition.**

Manuscript received 9 June 2022; revised 28 August 2022 and 14 October 2022; accepted 25 October 2022. Date of publication 24 November 2022; date of current version 6 December 2022. This work was supported in part by the National Natural Science Foundation of China under Grant 41604037 and Grant 41974061, in part by the Hubei Provincial Natural Science Foundation of China under Grant 2022CFB125, in part by the Open Funds of Key Laboratory of Exploration Technologies for Oil and Gas Resources (Yangtze University), Ministry of Education under Grant K2021-09, and in part by the Cooperative Innovation Center of Unconventional Oil and Gas (Ministry of Education and Hubei Province) under Grant UOG2020-09. *(Corresponding author: Na Fan.)*

Na Fan is with the Key Laboratory of Exploration Technology for Oil and Gas Resources of Ministry of Education, School of Geophysics and Oil Resources, Yangtze University, Wuhan 430100, China (e-mail: fanna@yangtzeu.edu.cn).

Xiao-Bi Xie is with the Institute of Geophysics and Planetary Physics, University of California Santa Cruz, Santa Cruz, CA 95064 USA (e-mail: xxie@ucsc.edu).

Lian-Feng Zhao and Zhen-Xing Yao are with the Key Laboratory of Earth and Planetary Physics, Institute of Geology and Geophysics, Chinese Academy of Sciences, Beijing 100029, China (e-mail: zhaolf@mail.iggcas.ac.cn; yaozx@mail.iggcas.ac.cn).

Xiyan Zhou is with the College of Geophysics, Chengdu University of Technology, Chengdu 610023, China (e-mail: zhouxiyan19@163.com).

Digital Object Identifier 10.1109/TGRS.2022.3224736

I. Introduction

MULTICOMPONENT imaging has long been an active research topic for exploration geophysicists because it can provide previously unavailable information and better constraints on the physical properties of subsurface targets compared to conventional single-component imaging. Decomposing the multicomponent elastic wavefield into P- and S-wave components is an important basis for processing elastic data and also a key step in elastic reverse time migration (ERTM) [1], [2], [3], [4], [5]. It facilitates the removal of crosstalk artifacts from the depth image, extracts additional information through interactions of different wave types, e.g., PP, PS, SS, and SP, and thus, provides better constraints to the subsurface attributes [2], [6], [7]. There are mainly two categories of elastic wavefield separation methods.

One method is the use of the divergence and curl operators based on Helmholtz's decomposition theorem [8]. By applying operators $\nabla\cdot$ and $\nabla\times$ to the originally coupled vector wavefield, the P and S wave modes can be separated [6], [7], [9], [10]. The amplitude, phase, dimension, and polarization of these separated waves are, however, different from those in the originally coupled wavefield, e.g., the vector particle displacement or velocity [3], [11]. If repeatedly using the gradient and curl operators, i.e., $\nabla(\nabla\cdot)$ and $\nabla\times(\nabla\times)$, to the originally coupled vector wavefield, separated vector P and S wavefields can be obtained, but the amplitude, phase, and dimension still need to be corrected [7], [12], [13], [14].

The divergence, curl, and gradient operations can be conducted in either spatial or wavenumber domains. For wavenumber domain operation, by using the normalized wavenumber, the above-mentioned amplitudes, phases, and dimension changes can be easily corrected [9], [12]. The

wavenumber domain operation, however, requires shuttling between the space and wavenumber domains at each time iteration; thus, for the commonly used time-space domain finite-difference (FD), method the computational cost is extremely high.

The wavefield separations can also be achieved in the spatial domain, which is often more computationally efficient; however, the related amplitude, phase, and dimension changes are more difficult to recover [15]. Applying the $\nabla\cdot$ and $\nabla\times$ operation each time will generate a $\pi/2$ phase shift and an amplitude change, which is inversely proportional to the local P or S velocity [16], [17]. To eliminate the phase change, Sun et al. [16] proposed to compensate for the phase shift using the Hilbert transform. Duan and Sava [7] introduced time integration or equivalently using a $1/i\omega$ filter in the Fourier domain to the source wavelet and receiver records before wavefield extrapolation. To remove amplitude changes, Sun et al. [17] proposed to multiply the separated S wave by a balancing factor, which is the S-to-P velocity ratio. Duan and Sava [7] used the local velocity to compensate for the amplitude of the separated P and S waves.

For P and S wavefields separated directly performing operations $\nabla(\nabla\cdot)$ and $\nabla\times\ (\nabla\times)$ in the space domain, they recover the vector property of the original wavefields, but their amplitudes, phases, and dimensions are all incorrect [7], [13], [18]. Zhu [18] achieved the amplitude- and phase-preserved wavefield by further solving a vector Poisson's equation with respect to the extrapolated vector wavefield, followed by decomposing the solved vector wavefields using $\nabla(\nabla\cdot)$ and $\nabla\times(\nabla\times)$; however, solving the Poisson's equation is rather costly, which limits its practical application in the ERTM. Yang et al. [14] proposed using a $1/\omega^2$ filter to modify the phases of the source wavelet and multicomponent records, as well as scale the amplitudes of extrapolated wavefields with the squares of P- and S-wave velocities $1/\alpha^2$ and $1/\beta^2$. This is equivalent to solving a vector Poisson's equation using an efficient way. The operators $\nabla(\nabla\cdot)$ and $\nabla\times\ (\nabla\times)$ are then applied to the amplitude- and phase-corrected vector wavefields to produce vector P and S waves.

Another commonly used wavefield separation method is solving the P- and S-wave decoupled elastic wave equations, either the second-order displacement equation [19] or the first-order velocity-stress elastic wave equation [20], [21], [22], [23]. This wavefield decoupling method can separate coupled wavefield into vector P and S waves while still preserving their phase and amplitude information, thus being widely used in the ERTM recently [23], [24], [25], [26], [27], [28], [29]. This type of elastic wavefield separation method, however, changes the form of the traditional coupled elastic wave equation. So it is usually not easy to expand to other complex media, such as with terrain, viscoelasticity or anisotropy, etc., whereas the separation method based on divergence and curl operators can be easily expanded to complex situations because these operators are directly performed to the originally coupled vector wavefield with no need to change the form of traditional coupled elastic wave equations.

In order to produce scalar imaging results, usually scalar or vector wavefields are extracted from the original elastic wavefield to represent P and S waves, and it is also better to preserve the amplitude and polarization information during wavefield separation. For scalar wavefields, scalar imaging conditions are usually used in ERTM. PP image can show true reflectivity imaging as long as the scalar P wave has the correct amplitude and phase information [26], [29]. But the PS image has two problems. One is that a scalar S wave converted from vector Helmholtz potential is difficult to obtain [3], [7], [11]. Another issue is that the P-to-S reflection exhibits a polarity reversal at normal incidence in isotropic media [30]. It can lead to problems when stacking PS images from multiple shots. Therefore, the polarity should be corrected before stacking [3], [7], [31], [32], [33], [34], [35]. Polarity correction is a complicated and time-consuming process and usually needs to introduce other parameters, such as the Poynting vector and interface information. If these parameters are inaccurate, it will affect the final imaging.

For vector wavefields, vector imaging conditions are widely used in ERTM. The dot-product vector imaging conditions are proposed by summing the dot product of the vector source and receiver wavefields [18], [22], [24], [36]. The imaging results are, however, undermined by the cosine or sine of the incident and reflection angles, which cannot represent the true reflectivity [26], [36]. Later, the magnitude- and sign-based vector imaging conditions [26] or called modified dot-product vector imaging conditions in Yang et al. [14]'s paper, are proposed by crosscorrelating the amplitudes from the vector source and receiver wavefield, whereas the sign was calculated through their dot-product results. This imaging condition can partially eliminate the effects produced by propagation angles. PP image still has the problem of polarity reversal when the opening angle is beyond 90° while the PS image is completely fine [26].

In this study, we propose a wavefield separation method based on the divergence and curl operations in the space domain, with all amplitude and phase corrections also conducted in the space domain. In addition to generating vector P and S waves with correct amplitude and phase, the proposed method also generated a special scalar P wave, which is the projection of the vector P wave in the propagation direction. It can be directly used in the ERTM to generate the PP image. On the other hand, the vector P and S waves can be used to generate the PS image.

II. Theory

A. Wavefield Separation

In an isotropic medium, elastic wavefield can be separated using the Helmholtz decomposition [8], [9], i.e., its compressional component P and shear component $\mathbf{S}$ can be obtained by applying the divergence and curl operators to the original vector wavefield $\mathbf{U}$

$$\begin{aligned} P &= \nabla\cdot\mathbf{U} \\ \mathbf{S} &= \nabla\times\mathbf{U} \end{aligned} \tag{1}$$

where the vector wavefield $\mathbf{U}$ can either be displacement or particle velocity, P is a scalar, and $\mathbf{S}$ is a vector perpendicular to the S-wave polarization. In the wavenumber domain,

(1) can be transformed to

$$\hat{P} = i\mathbf{k}\cdot\hat{\mathbf{U}} = ik\left(\mathrm{I}\cdot\hat{\mathbf{U}}\right)$$
$$\hat{\mathbf{S}} = i\mathbf{k}\times\hat{\mathbf{U}} = ik\left(\mathbf{I}\times\hat{\mathbf{U}}\right) \tag{2}$$

where the hat $\wedge$ denotes the corresponding variables in the wavenumber domain, $\mathbf{k}$ is the wavenumber vector, which parallels the wave propagation direction and also the P-wave-polarization direction, $k = |\mathbf{k}| = \omega/v$ is its modulus, and v is the phase velocity, ω is the angular frequency. $\mathbf{I} = \mathbf{k}/k$ is the unit vector along the propagation direction. The decomposed wavefields have their amplitudes, phases, and physical dimensions changed compared to the original wavefield. The factor ik introduces a $\pi/2$-phase shift and changes the P- and S-wave amplitudes by a factor that is inversely proportional to the P and S velocity, respectively [16], [17].

Next, let

$$\hat{P}^{cor} = \mathrm{I}\cdot\hat{\mathbf{U}}$$
$$\hat{\mathbf{S}}^{cor} = \mathbf{I}\times\hat{\mathbf{U}} \tag{3}$$

where $\hat{P}^{cor}$ and $\hat{\mathbf{S}}^{cor}$ are the amplitude- and phase-corrected $\hat{P}$ and $\hat{\mathbf{S}}$. Substituting (3) into (2) and replacing k by k_P and k_S for P and S wave, respectively, we have

$$\hat{P}^{cor} = \frac{\hat{P}}{ik_P}$$
$$\hat{\mathbf{S}}^{cor} = \frac{\hat{\mathbf{S}}}{ik_S}. \tag{4}$$

Compared to the originally decomposed wavefields in (1), the wavefields in (4) have correct amplitudes, phases, and dimensions. P^{cor} is a scalar wave and can be regarded as the vector P wave projected to its propagation direction. P^{cor} and $\mathbf{S}^{cor}$ should have the equal energies with $\mathbf{U}$.

In addition, these waves have dispersion relations $k_P = \omega/\alpha$ for P-wave and $k_S = \omega/\beta$ for S-wave in an isotropic elastic medium, where α and β are the P- and S-wave velocities, respectively. Substituting them into (4), we obtain

$$\hat{P}^{cor} = \frac{\alpha}{i\omega}\,\hat{P}$$
$$\hat{\mathbf{S}}^{cor} = \frac{\beta}{i\omega}\hat{\mathbf{S}}. \tag{5}$$

Transforming them back to the time-space domain, we have

$$\frac{\partial P^{cor}}{\partial t} = \alpha P = \alpha\nabla\cdot\mathbf{U}$$
$$\frac{\partial\mathbf{S}^{cor}}{\partial t} = \beta\mathbf{S} = \beta\nabla\times\mathbf{U}. \tag{6}$$

Finally, (6) can be used for correcting the phase and amplitude of the separated Helmholtz potential wavefields in the time-space domain.

To recover the vector polarization information, the wavenumber domain equation is [12]

$$\hat{\mathbf{U}}^P = \mathrm{I}\left(\mathrm{I}\cdot\hat{\mathbf{U}}\right)$$
$$\hat{\mathbf{U}}^S = -\mathbf{I}\times\left(\mathbf{I}\times\hat{\mathbf{U}}\right) \tag{7}$$

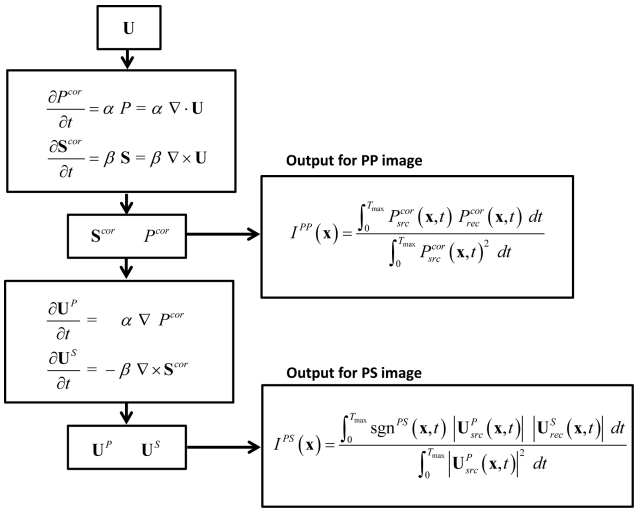

Fig. 1. Flowchart for P- and S-wave decomposition and ERTM.

where $\mathbf{U}^P$ is the vector P wave and $\mathbf{U}^S$ is the vector S wave. Substituting (3) into (7), we obtain

$$\hat{\mathbf{U}}^P = \mathrm{I}\;\hat{P}^{cor}$$
$$\hat{\mathbf{U}}^S = -\mathbf{I}\times\hat{\mathbf{S}}^{cor}. \tag{8}$$

Similar to the amplitude- and phase-correction process described in (3) to (6), we have

$$\frac{\partial\mathbf{U}^P}{\partial t} = \alpha\nabla P^{cor}$$
$$\frac{\partial\mathbf{U}^S}{\partial t} = -\beta\,\nabla\times\mathbf{S}^{cor}. \tag{9}$$

Finally, the correct vector P and S waves can be obtained from the original elastic wavefield through two successive steps, i.e., (6) and (9). The flowchart of wavefield separation is illustrated in Fig. 1. Here, the vector polarization is obtained by repeatedly using divergence and curl operations; the amplitude corrections are done by multiplying local P and S wave velocities. The two time derivatives are reversed by solving two partial differential equations. The entire process can be conveniently embedded in commonly used space-time FD methods. The processes of solving (6) and (9) using the FD scheme are presented in Appendixes B and C.

B. Elastic Reverse-Time Migration

We mainly focus on the PP and PS images. Considering that a normalized cross-correlation image condition, including the source-side illumination, can provide correct angle dependence, scale factor, sign, and the required dimensionless units [4], we adopt a normalized cross-correlation image condition. There are three kinds of popular imaging conditions. The first one is the scalar imaging condition [6], [7]

$$I^{PP}(\mathbf{x}) = \frac{\int_0^{T_{\max}} P^{cor}_{src}(\mathbf{x},t)\,P^{cor}_{rec}(\mathbf{x},t)\;dt}{\int_0^{T_{\max}} P^{cor}_{src}(\mathbf{x},t)^2\;dt}$$
$$I^{PS}(\mathbf{x}) = \frac{\int_0^{T_{\max}} P^{cor}_{src}(\mathbf{x},t)\,S^{cor}_{rec}(\mathbf{x},t)\;dt}{\int_0^{T_{\max}} P^{cor}_{src}(\mathbf{x},t)^2\;dt}. \tag{10}$$

The second one is the dot-product vector imaging condition [18], [36]

$$I^{PP} = \frac{\int_0^{T_{\max}} \mathbf{U}^P_{src} \cdot \mathbf{U}^P_{rec}\, dt}{\int_0^{T_{\max}} \left|\mathbf{U}^P_{src}(\mathbf{x},t)\right|^2 dt}$$
$$I^{PS} = \frac{\int_0^{T_{\max}} \mathbf{U}^P_{src} \cdot \mathbf{U}^S_{rec}\, dt}{\int_0^{T_{\max}} \left|\mathbf{U}^P_{src}(\mathbf{x},t)\right|^2 dt}. \tag{11}$$

The last one is the magnitude- and sign-based vector imaging condition [14], [26]

$$I^{PP}(\mathbf{x}) = \frac{\int_0^{T_{\max}} \mathrm{sgn}^{PP}(\mathbf{x},t)\left|\mathbf{U}^P_{src}(\mathbf{x},t)\right|\left|\mathbf{U}^P_{rec}(\mathbf{x},t)\right| dt}{\int_0^{T_{\max}} \left|\mathbf{U}^P_{src}(\mathbf{x},t)\right|^2 dt}$$
$$I^{PS}(\mathbf{x}) = \frac{\int_0^{T_{\max}} \mathrm{sgn}^{PS}(\mathbf{x},t)\left|\mathbf{U}^P_{src}(\mathbf{x},t)\right|\left|\mathbf{U}^S_{rec}(\mathbf{x},t)\right| dt}{\int_0^{T_{\max}} \left|\mathbf{U}^P_{src}(\mathbf{x},t)\right|^2 dt} \tag{12}$$

where I^{PP} and I^{PS} are PP and PS images, the subscripts *src* and *rec* denote the source and receiver wavefields, the operator "$\cdot$" denotes the dot product between two vectors and $|\cdot|$ denotes taking the amplitude of a vector. sgn^{PP} and sgn^{PS} can be calculated by [14], [26]

$$\mathrm{sgn}^{PP}(\mathbf{x},t) = \begin{cases} +1 & \mathbf{U}^P_{src}(\mathbf{x},t)\cdot\mathbf{U}^P_{rec}(\mathbf{x},t) > 0 \\ -1 & \mathbf{U}^P_{src}(\mathbf{x},t)\cdot\mathbf{U}^P_{rec}(\mathbf{x},t) < 0 \end{cases}$$
$$\mathrm{sgn}^{PS}(\mathbf{x},t) = \begin{cases} +1 & \mathbf{U}^P_{src}(\mathbf{x},t)\cdot\mathbf{U}^S_{rec}(\mathbf{x},t) > 0 \\ -1 & \mathbf{U}^P_{src}(\mathbf{x},t)\cdot\mathbf{U}^S_{rec}(\mathbf{x},t) < 0. \end{cases} \tag{13}$$

But PS scalar imaging condition in (10) has a polarity reversal problem at normal incidence in 2-D media. The dot-product imaging condition in (11) underestimates the true reflectivity by the cosine or sine of the incident and reflection angles. The last imaging condition for the PP image has the polarity-reversal problem when the opening angle is beyond 90° while the PS image is completely fine. So we use a combination of scalar and vector imaging conditions, where a PP image is produced by the scalar imaging condition and a PS image by the magnitude- and sign-based vector imaging condition.

$$I^{PP}(\mathbf{x}) = \frac{\int_0^{T_{\max}} P^{cor}_{src}(\mathbf{x},t) P^{cor}_{rec}(\mathbf{x},t)\, dt}{\int_0^{T_{\max}} P^{cor}_{src}(\mathbf{x},t)^2\, dt}$$
$$I^{PS}(\mathbf{x}) = \frac{\int_0^{T_{\max}} \mathrm{sgn}^{PS}(\mathbf{x},t)\left|\mathbf{U}^P_{src}(\mathbf{x},t)\right|\left|\mathbf{U}^S_{rec}(\mathbf{x},t)\right| dt}{\int_0^{T_{\max}} \left|\mathbf{U}^P_{src}(\mathbf{x},t)\right|^2 dt}. \tag{14}$$

The ERTM workflow can be summarized as below (Fig. 1):

1) Calculating the source wavefield $\mathbf{U}_{src}$ by solving the elastic-wave equation using, e.g., the FD code. Use the method described in Appendixes B and C to solve (6) and obtain source-side corrected scalar wavefield P^{cor}_{src}. Use the method described in Appendixes to solve (6) and (9) to obtain vector P wavefield $\mathbf{U}^P_{src}$.

2) Calculating the receiver wavefield $\mathbf{U}_{rec}$ by solving the adjoint elastic-wave equation. Similarly, using the methods described in Appendixes B and C, solve (6) and (9) to obtain receiver-side wavefields P^{cor}_{rec}, $\mathbf{S}^{cor}_{rec}$, and $\mathbf{U}^S_{rec}$.

3) Apply the elastic imaging condition (14) to produce PP- and PS-reflectivity images.

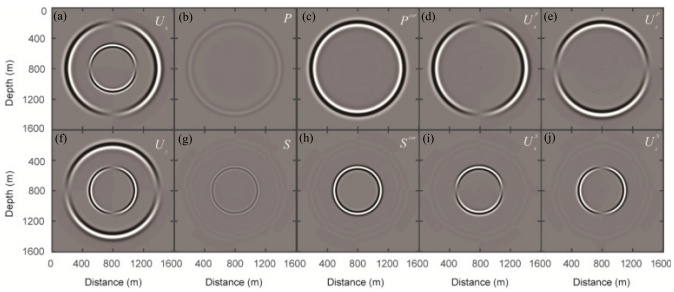

Fig. 2. Snapshots at 0.24 s in a homogenous model. (a) and (f) Are horizontal and vertical components (U_x and U_z) of coupled vector wavefield. (b) and (g) Are Helmholtz potential wavefields (P and S) separated by traditional Helmholtz decomposition. (c) and (h) Are amplitude- and phase-corrected wavefields P^{cor} and S^{cor} from (6). (d), (e), (i), and (j) Are horizontal and vertical components of vector P and S wavefields (U^P_x, U^P_z, U^S_x, and U^S_z) calculated by (9).

Note that there are two types of FD calculations involved. The first is for updating the main source and receiver side wavefields $\mathbf{U}_{src}$ and $\mathbf{U}_{rec}$. The second is embedded in every time-iteration step to separate coupled elastic waves into P and S waves.

We also compare the commonly used ERTM methods in Appendix A and list the detailed wavefield separation methods and the corresponding PP and PS imaging conditions.

III. Examples

A. 2-D Homogeneous Models

In this section, we present three numerical experiments to validate the proposed elastic wavefield decomposition and ERTM workflow in 2-D models.

In the first example, we validate the wavefield separation method using a homogeneous model with a size of 1600×1600 m^2 and velocities of $\alpha = 3000$ m/s and $\beta = 1500$ m/s. A dipole source radiating both P and S waves and having a 25-Hz Ricker wavelet is injected at (800 m, 800 m). A receiver is placed at (534 m, 400 m). A fourth-order regular-grid FD scheme is used to solve the 2-D second-order displacement elastic-wave equation and simulate the propagation of P-SV waves. The PML absorbing boundary condition [37] is used for all boundaries. We show the snapshots at 0.24 s in Fig. 2. Fig. 2(a) and (f) are horizontal and vertical components (U_x and U_z) of the coupled vector wavefield $\mathbf{U}$. Fig. 2(b) and (g) are Helmholtz potential wavefields (P and S) separated by Helmholtz decomposition using the divergence and curl operators. Fig. 2(c) and (h) are amplitude- and phase-corrected Helmholtz potential wavefields (P^{cor} and S^{cor}) calculated in (6). Note, in 2-D, the S^{cor} has only one component. Fig. 2(d), (e), (i), and (j) are horizontal and vertical components of vector P and S wavefields (U^P_x, U^P_z, U^S_x, and U^S_z) calculated by (9). We also compare their waveforms and energies from a receiver located at (534 m, 400 m). Figs. 3 and 4 compare waveforms of coupled vector wavefield, uncorrected and corrected separated Helmholtz potential wavefields, and decoupled vector P and S wavefields. Black solid and dashed lines are U_x and U_z. Blue solid and dashed lines are P and S. Red solid and dashed

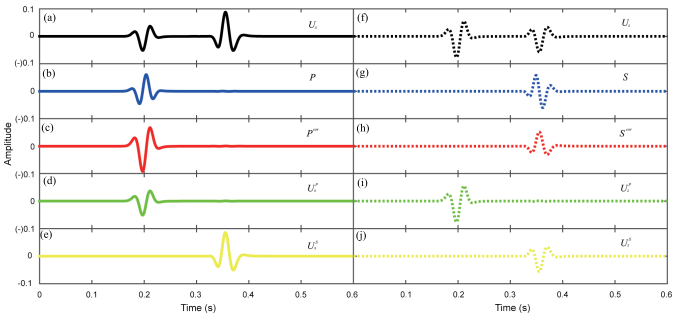

Fig. 3. Waveforms at a receiver location (534 , 400). (a)–(j) Are corresponded to the snapshots in Fig. 2.

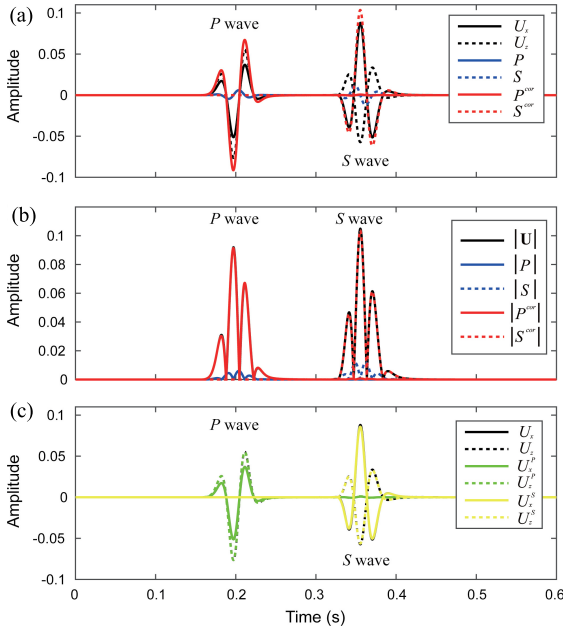

Fig. 4. Waveform comparisons at a receiver location (534, 400). (a) Comparisons among coupled vector wavefield, decomposed and corrected Helmholtz potential wavefields. Black solid and dashed lines are U_x and U_z. Blue solid and dashed lines are P and S. Red solid and dashed lines are P^{cor} and S^{cor}. (b) Modules of individual vector or scalar waveforms. Black solid line is for coupled vector wavefield $|\mathbf{U}|$. Blue solid and dashed lines are for $|P|$ and $|S|$. Red solid and dashed lines are for $|P^{cor}|$ and $|S^{cor}|$. (c) Comparisons of waveforms between the coupled vector wavefield and decomposed vector P- and S-wavefields. Green solid and dashed lines are for U_x^P and U_z^P. Yellow solid and dashed lines are for U_x^S and U_z^S.

lines are P^{cor} and S^{cor}. Green solid and dashed lines are U_x^P and U_z^P. Yellow solid and dashed lines are U_x^S and U_z^S. We draw the waveforms separately in Fig. 3 for clear display and overlap them in Fig. 4(a) and (c) for comparison. In order to check their energy, we calculate magnitudes of vector and scalar waveforms and compare them in Fig. 4(b). Black solid line is the modulus of coupled vector wavefield $|\mathbf{U}|$. Blue solid and dashed lines are $|P|$ and $|S|$. Red solid and dashed lines are $|P^{cor}|$ and $|S^{cor}|$. It show $P^{cor}(\mathbf{x},t)^2 = |\mathbf{U}^P(\mathbf{x},t)|^2$ and $S^{cor}(\mathbf{x},t)^2 = |\mathbf{U}^S(\mathbf{x},t)|^2$.

From these three figures, we see that the separated Helmholtz potential wavefields based on the divergence and curl operations do not preserve correct amplitudes and phases as in the originally coupled wavefields and lose their physical

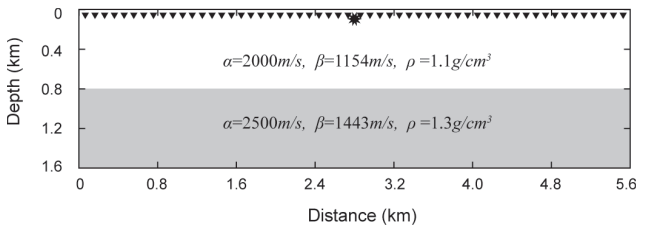

Fig. 5. Two-layer velocity model. The model size is 5600 × 1600^2, with its P- and S-wave velocities and densities are labeled in the figure.

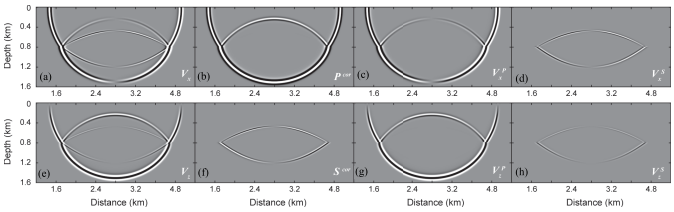

Fig. 6. Snapshots at 0.7 s in the two-layer model. (a) and (e) Horizontal and vertical components of the coupled vector wavefield. (b) and (f) Amplitude- and phase-corrected Helmholtz potential wavefields decomposed using (6). (c), (g), (d), and (h) Horizontal and vertical components of vector P and S wavefields calculated using (9).

interpretation. After amplitude and phase correction, the right amplitudes and phases are recovered and can be physically understood as the original P and S waves projected on the propagation direction and the direction perpendicular to the propagation direction. Both the separated vector P and S waves have the same amplitudes, phases, and vector polarizations as in the originally coupled vector wavefield.

B. 2-D Layered Model

In the second example, we verify the wavefield separation method and ERTM using a two-layer model (Fig. 5). The model has a size of 5600 × 1600 m^2 and velocities of $\alpha = 2000$ m/s, $\beta = 1154$ m/s, and $\rho = 1.1$ g/cm^3 in the top layer and $\alpha = 2500$ m/s, $\beta = 1443$ m/s, and $\rho = 1.3$ g/cm^3 in the bottom layer (Fig. 5). In order to compare the image quality, we calculate the image from one shot. An explosion source is placed at (2800 m, 40 m). A fourth-order staggered-grid FD scheme is used to solve the 2-D first-order particle-velocity elastic-wave equation. Fig. 6 illustrates the wavefield snapshots at 0.7 s. Fig. 6(a) and (e) are horizontal and vertical components (V_x and V_z) of coupled vector velocity wavefields. Fig. 6(b) and (f) are amplitude- and phase-corrected Helmholtz potential wavefields (P^{cor} and S^{cor}) separated using (6). Fig. 6(c), (d), (g), and (h) are horizontal and vertical components of vector P and S wavefields (V_x^P, V_z^P, V_x^S, and V_z^S) calculated using (9).

Three types of imaging conditions are used to produce PP and PS images, including scalar imaging conditions in (10) [Fig. 7(a) and (b)], dot-product vector imaging conditions in (11) [Fig. 7(c) and (d)] and magnitude- and sign-based vector imaging conditions in (12) [Fig. 7(e) and (f)]. We calculate the PP and PS amplitude versus angle curves in Fig. 8 for three different imaging conditions by extracting the maximum imaging amplitude from a small window of the first layer.

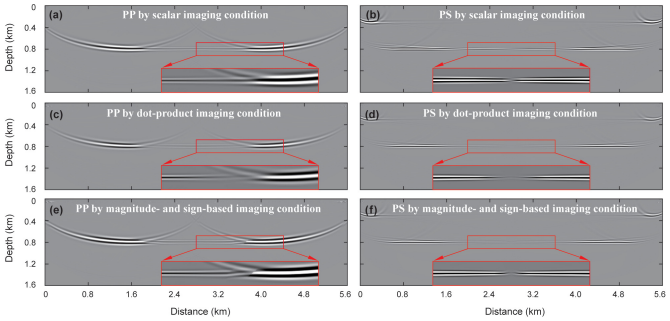

Fig. 7. PP and PS images from a single shot in the two-layer model. (a) and (b) PP and PS images using the scalar imaging conditions. (c) and (d) Images using the dot-product vector imaging conditions. (e) and (f) Images using the magnitude- and sign-based imaging condition.

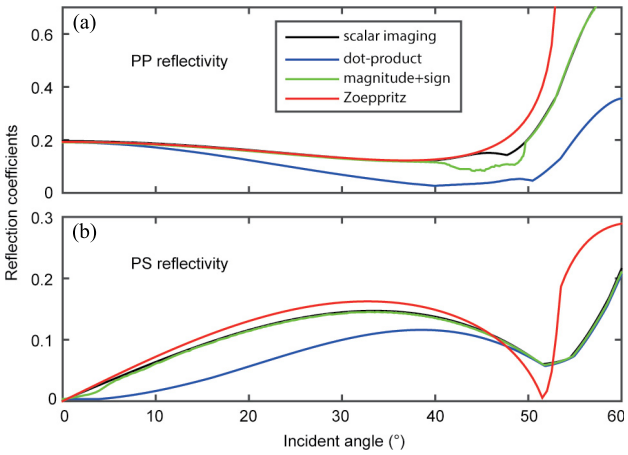

Fig. 8. (a) PP and (b) PS reflection coefficients verse angle of the velocity interface calculated by the scalar imaging condition (black lines), dot product imaging condition (blue lines), magnitude- and sign-based imaging condition (green lines) and the Zoeppritz equation (red lines).

We also calculate the true reflection coefficients by solving the Zoeppritz equation, which is a reference curve in Fig. 8. It only represents the correct amplitude of reflection coefficients but no polarity information. In this example, just for one single shot, interfaces with large offsets usually cannot be imaged to the correct positions, which are curved upside on both sides in Fig. 7. So the reflectivity amplitudes estimated from the large incident angle are also inaccurate. In practice, we stack the multishot images to eliminate the underestimated reflectivities from the large incident angle.

For PP images, the results by vector dot-product imaging condition are weakened, especially near the incident angle of 45°, and the polarity is reversed when the incident angle is greater than 45° [Figs. 7(c) and 8(a)]. The image by a magnitude- and sign-based imaging condition is not weakened by the incident angle, but the polarity reversal still exists when the incident angle is greater than 45° [Figs. 7(e) and 8(a)]. Only the scalar PP imaging condition gives the correct result [Figs. 7(a) and 8(a)]. For PS images, the scalar imaging condition has polarity reversal separated from the normal incidence [Fig. 7(b)]. The dot-product vector imaging condition has no polarity-reversal problem but weakens the reflectivity, especially near the normal incidence [Figs. 7(d) and 8(b)]. Only the PS image by a magnitude- and sign-based imaging condition gives the correct image [Figs. 7(f) and 8(b)]. Therefore, we propose to use a combination of scalar imaging conditions for the PP image and magnitude- and sign-based vector imaging conditions for the PS image, as described in (14) [Fig. 7(a) and (f)].

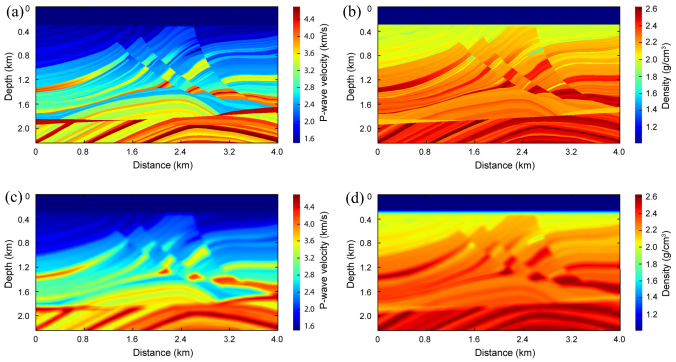

Fig. 9. Marmousi2 velocity model. (a) P-wave velocity (km/s), (b) density (g/cm^3), (c) smoothed P-wave velocity, and (d) density.

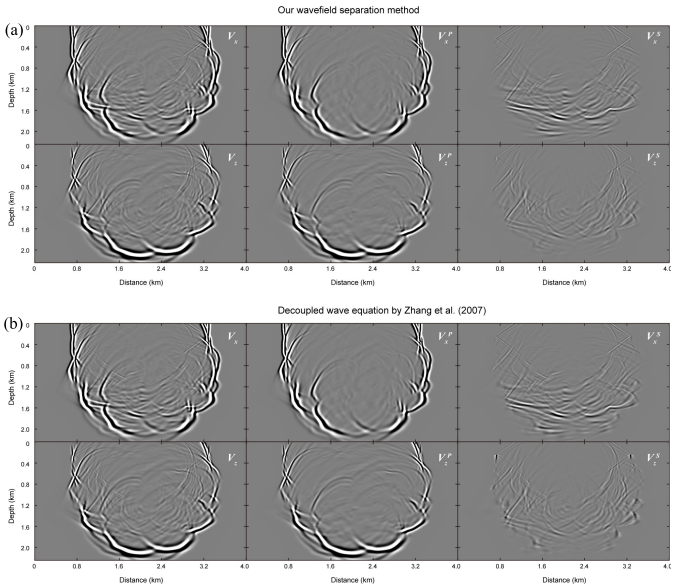

Fig. 10. Wavefield snapshots comparisons between (a) our wavefield separation method and (b) the decoupled elastic-wave equation by Zhang et al. [21]. Six panels in (a) and (b) are the snapshots of horizontal and vertical components of coupled vector particle-velocity wavefields (V_x and V_z) and decoupled vector P and S wavefields (V_x^P, V_z^P, V_x^S, and V_z^S) at the time instant of 0.9 s.

C. 2-D Marmousi2 Velocity Model

In the last example, we test the wavefield decomposition and ERTM in the Marmousi2 velocity model [Fig. 9(a) and (b)] [38]. The S-wave velocity is derived from the P-wave velocity according to $\beta = \alpha/(3)^{1/2}$. There are 99 explosive sources with a 25-Hz Ricker wavelet located at the surface from a distance of 40 to 3964 m with a shot spacing of 40 m. The migration velocity model is smoothed from the true model, as shown in Fig. 9(c) and (d). To verify the correctness of our wavefield decomposition method in heterogenous media,

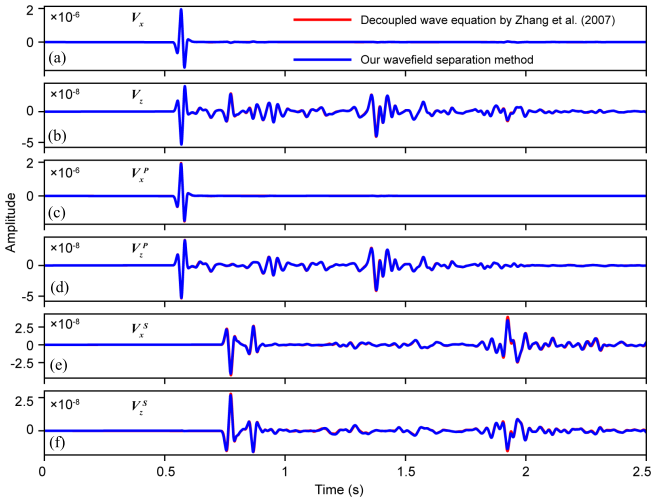

Fig. 11. Waveforms comparisons at the same location between our wavefield separation method (blue lines) and the decoupled elastic-wave equation by Zhang et al. [21] (red lines). (a)–(f) Show the horizontal and vertical components of coupled vector particle-velocity wavefields (V_x and V_z) and decoupled vector P and S wavefields (V_x^P, V_z^P, V_x^S, and V_z^S), respectively.

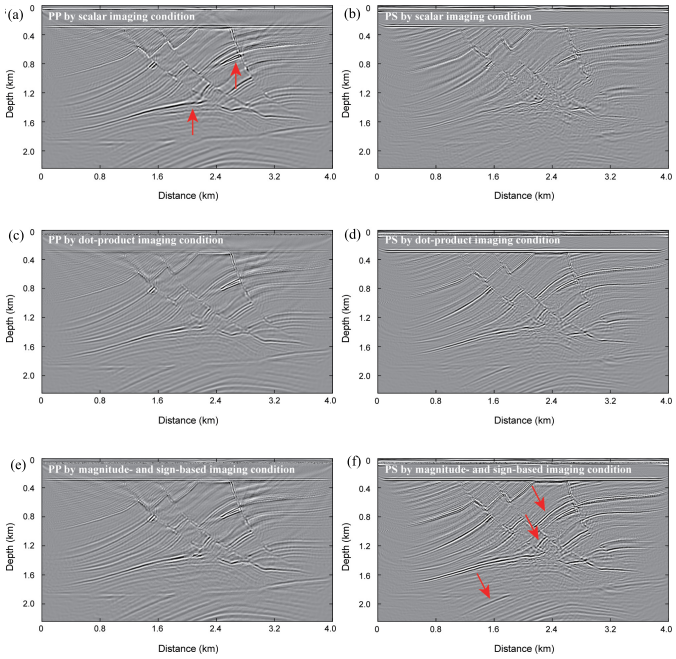

Fig. 12. PP and PS images in the Marmousi2 model. (a) and (b) PP and PS images using the scalar imaging conditions. (c) and (d) Using the dot-product vector imaging conditions. (e) and (f) Using the magnitude- and sign-based imaging condition.

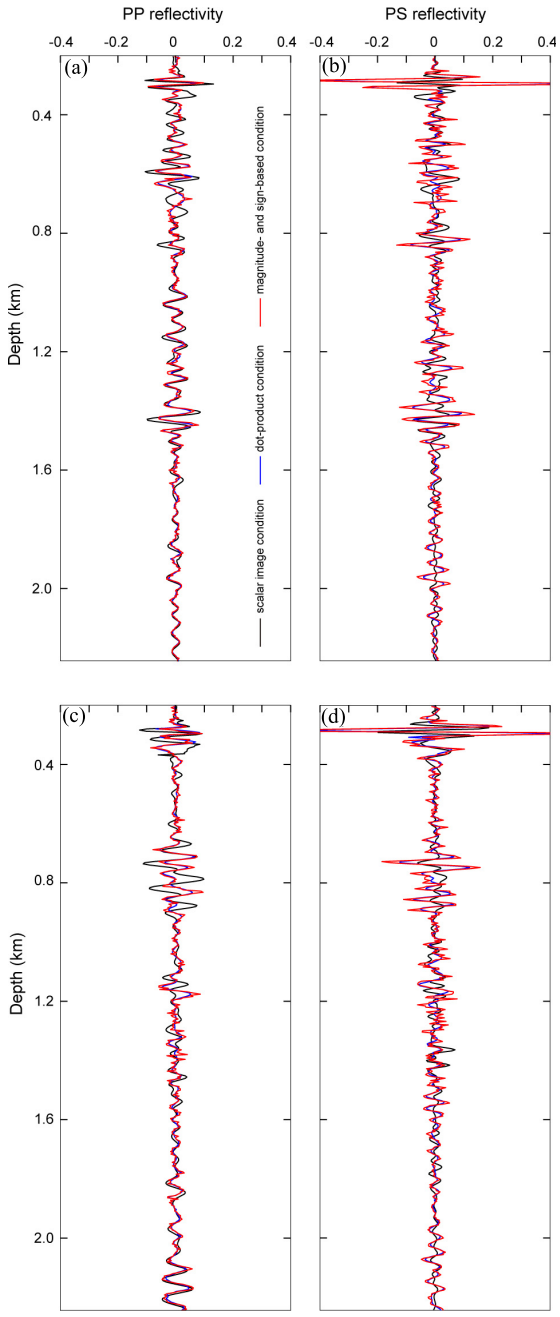

Fig. 13. Comparisons of traces in the (a) and (c) PP and (b) and (d) PS images in the Marmousi2 model at a horizontal distance (a) and (b) 1.6 km and (c) and (d) 2.4 km. The black lines are from images using scalar imaging conditions. The blue lines are from images using dot-product vector imaging conditions. The red lines are from images using magnitude- and sign-based vector imaging conditions.

in Figs. 10 and 11, we compare the results with that from the decoupled first-order velocity-stress elastic wave equation in [21]. Fig. 11 shows the coupled and decoupled vector wavefield snapshots at the same time instant, and Fig. 12 shows the waveforms at the same receiver. We can see that the waveforms from the two wavefield decomposition methods are highly similar. Fig. 12 demonstrates the PP and PS images, where Fig. 12(a) and (b) are PP and PS images using the scalar wave imaging condition in (10), Fig. 12(c) and (d) are using dot-product vector imaging conditions in (11), and Fig. 12(e) and (f) are using magnitude- and sign-based vector imaging conditions in (12). Fig. 13 compares the PP [Fig. 13(a) and (c)] and PS [Fig. 13(b) and (d)] reflectivities at the distance of 1.6 km [Fig. 13(a) and (b)] and 2.4 km [Fig. 13(c) and (d)]. PP images from all three imaging conditions give good resolutions for complex structures in the entire depth range. PP and PS images from the dot-product vector imaging conditions are very close to those from the magnitude- and sign-based vector imaging conditions

but have slightly smaller amplitudes due to the effects of the cosine or sine of the opening angle between the incident and reflected waves; however, they are still different from the images using scalar imaging conditions. PP images using these two vector imaging conditions still have some amplitude and phase differences comparing to the image from scalar imaging conditions, especially in the shallow depth, because the super-wide opening angles at large offset cause the problem of polarity reversal. For PS images, some complex structures cannot be correctly imaged using the PS scalar imaging condition because of the uncorrected polarity-reversal problem of the S wave. Therefore, PP from scalar imaging conditions and PS from magnitude- and sign-based vector imaging conditions can be used to represent the elastic true reflectivity images.

IV. Conclusion

The P- and S-wave decomposition based on divergence and curl operations can separate the P and S wave modes in isotropic elastic media but changes the amplitudes, phases, and dimensions compared to those in the original wavefield. We propose an amplitude- and phase-correction method, which can be conveniently achieved in the time-space domain and embedded in most of the time-domain FD propagators. The corrections to the distorted decomposed P and S wavefields are organized into two differential equations. By solving these two equations, the separated P and S wavefields can recover the correct amplitude, phase, and vector polarizations as in the originally coupled wavefield. The detailed procedurals for solving these decomposition equations are given in Appendixes B and C. We then apply the separated P and S wavefields in the ERTM workflow. For the PP image, we propose to use the scalar imaging condition by crosscorrelating the scalar Helmholtz potential wavefields generated during the decomposition for both source and receiver wavefields. For the PS image, we propose to use the magnitude- and sign-based vector imaging condition, i.e., crosscorrelating the magnitudes of the source-side P-wave and the receiver-side S-wave, whereas the sign is calculated through their dot-product results. Finally, we use three 2-D numerical examples to validate the elastic wavefield separation and apply them in the ERTM for the PP- and PS-reflectivity images, although the formulations are for full 3-D.

The ERTM method is conducted in isotropic elastic media; however, the idea can still be easily expanded to other complex media, such as with terrain, viscoelasticity, anisotropy, etc., because the wavefield separation expressions based on divergence and curl operators are directly performed to the originally coupled vector wavefield, and we do not need to change the form of traditionally coupled elastic wave equation.

Appendix

A. Comparisons of Different ERTM Methods

We list the commonly used methods of wavefield separation and the corresponding imaging conditions to produce PP and PS images in Table I. For convenience in writing the source-normalized zero-lag cross-correlation imaging condition, we omit the source-normalized term. Methods 1–6 can be applied to displacement or particle-velocity wavefield. Methods 7 and 8 are used in the velocity-stress equation. Method 1 is used in the divergence and curl operators based on Helmholtz's decomposition theorem to separate the P and S wavefield. Methods 2–4 are all using the $\nabla(\nabla\cdot)$ and $\nabla\times(\nabla\times)$ operators; however, by directly applying these operators to the original wavefield, one can obtain the separated vector wavefield with distorted amplitude and phase. So methods 3 and 4 are applyed to the modified original wavefield, and then P and S wave with correct amplitude and phase can be decomposed. Although methods 3, 4, and 6 can decompose the P and S wave, the imaging conditions, especially for the PP image cannot represent the true reflectivity. In method 7, the auxiliary P-wave stress wavefield τ^P is introduced to generate a P-wave stress image to replace the PP image. But τ^P is not exactly equal to the scalar P-wave particle-velocity wavefield and the P-wave stress image has a different physical meaning from the PP image. In our method, if we define $\mathbf{U}$ to be particle-velocity wavefield and then compare with method 7, we have the following relation:

$$P^{cor} = \frac{1}{\sqrt{\rho(\lambda+2\mu)}}\tau^P. \tag{A1}$$

We can see the P-wave stress wavefield divided by the elastic impedance of the media can be converted to the scalar P-wave particle-velocity wavefield. In method 8, Zhou et al. [26] define the scalar P-wave particle velocity wavefield as $\bar{v}_P$ and give the different expressions in 2-D and 3-D media. Compared with our method, we find $P^{cor} = \bar{v}_P$ for either 2-D or 3-D case. But their scalar P-wave particle-velocity wavefield are obtained based on the stress wavefield and only applied for decoupled velocity-stress equation. Our method can be applied to both displacement and velocity-stress equation. P^{cor} can denote either the scalar P-wave particle-velocity or displacement wavefield.

B. FD Schemes for P and S Wave Decomposition in 3-D Medium

We present two types of FD schemes for P and S wave decomposition in 3-D medium. One is using regular-grid FD scheme to solve the second-order displacement elastic-wave equation, and the other is using the staggered-grid FD scheme to solve the first-order particle-velocity elastic-wave equation. We first expand (6) and (9) for calculating the corrected Helmholtz potential wavefields and vector wavefields. Equation (6) can be expressed by

$$\begin{aligned}
&\frac{\partial P^{cor}}{\partial t} = \alpha\left(\frac{\partial U_x}{\partial x}+\frac{\partial U_y}{\partial y}+\frac{\partial U_z}{\partial z}\right)\\
&\begin{cases}
\dfrac{\partial S_x^{cor}}{\partial t} &= \beta\left(\dfrac{\partial U_z}{\partial y}-\dfrac{\partial U_y}{\partial z}\right)\\
\dfrac{\partial S_y^{cor}}{\partial t} &= \beta\left(\dfrac{\partial U_x}{\partial z}-\dfrac{\partial U_z}{\partial x}\right)\\
\dfrac{\partial S_z^{cor}}{\partial t} &= \beta\left(\dfrac{\partial U_y}{\partial x}-\dfrac{\partial U_x}{\partial y}\right)
\end{cases}
\end{aligned} \tag{B1}$$

TABLE I
COMPARISONS OF COMMONLY USED ERTM METHODS

	Wavefield separation	Imaging conditions	Main references	Descriptions
1	$P = \nabla \cdot \mathbf{U}$ $\mathbf{S} = \nabla \times \mathbf{U}$	$I^{PP} = \int P_{src}\ P_{rec}\ dt$ $I^{PS} = \int P_{src}\ \mathbf{S}_{rec}\ dt$ $\left(\text{or } I^{PS} = \int (\nabla P_{src} \times \mathbf{n}) \cdot \mathbf{S}_{rec}\ dt \right)$	Yan and Sava, 2008; Duan and Sava, 2015	P and $\mathbf{S}$ are the scalar and vector potential wavefields respectivly.
2	$\bar{\mathbf{U}}^P = \nabla(\nabla \cdot \mathbf{U})$ $\bar{\mathbf{U}}^S = -\nabla \times (\nabla \times \mathbf{U})$	$I^{PP} = \int \bar{\mathbf{U}}^P_{src} \cdot \bar{\mathbf{U}}^P_{rec}\ dt$ $I^{PS} = \int \bar{\mathbf{U}}^P_{src} \cdot \bar{\mathbf{U}}^S_{rec}\ dt$	Li et al., 2016	$\bar{\mathbf{U}}^P$ and $\bar{\mathbf{U}}^S$ are the vector wavefields but with distorted amplitude and phase.
3	$\nabla^2 \mathbf{W} = \mathbf{U}$ $\mathbf{U}^P = \nabla(\nabla \cdot \mathbf{W})$ $\mathbf{U}^S = -\nabla \times (\nabla \times \mathbf{W})$	$I^{PP} = \int \mathbf{U}^P_{src} \cdot \mathbf{U}^P_{rec}\ dt$ $I^{PS} = \int \mathbf{U}^P_{src} \cdot \mathbf{U}^S_{rec}\ dt$	Zhu, 2017	$\mathbf{U}^P$ and $\mathbf{U}^S$ are the vector wavefields with preserving the original amplitude and phase information.
4	$\mathbf{U}^P = \nabla\left(\nabla\alpha^2 \cdot F^{-1}\left(-\frac{\mathbf{U}}{\omega^2} \right) \right)$ $\mathbf{U}^S = -\nabla \times \left(\beta^2 \nabla \times F^{-1}\left(-\frac{\mathbf{U}}{\omega^2} \right) \right)$	$I^{PP} = \int \text{sgn}^{PP}\ \left\lvert \mathbf{U}^P_{src} \right\rvert\ \left\lvert \mathbf{U}^P_{rec} \right\rvert\ dt$ $I^{PS} = \int \text{sgn}^{PS}\ \left\lvert \mathbf{U}^P_{src} \right\rvert\ \left\lvert \mathbf{U}^S_{rec} \right\rvert\ dt$	Yang et al., 2018	F^{-1} denotes the inverse Fourier transform.
5	$\frac{\partial P^{cor}}{\partial t} = \alpha\ \nabla \cdot \mathbf{U}$ $\frac{\partial \mathbf{S}^{cor}}{\partial t} = \beta\ \nabla \times \mathbf{U}$ $\frac{\partial \mathbf{U}^P}{\partial t} = \alpha\ \nabla\ P^{cor}$ $\frac{\partial \mathbf{U}^S}{\partial t} = -\beta\ \nabla \times \mathbf{S}^{cor}$	$I^{PP} = \int P^{cor}_{src}\ P^{cor}_{rec}\ dt$ $I^{PS} = \int \text{sgn}^{PS}\ \left\lvert \mathbf{U}^P_{src} \right\rvert\ \left\lvert \mathbf{U}^S_{rec} \right\rvert\ dt$	This study	P^{cor} and $\mathbf{S}^{cor}$ are the amplitude- and phase-corrected scalar and vector potential wavefields. P^{cor} also denotes the scalar P-wave particle-velocity or displacement wavefield.
6	$\frac{\partial^2 \mathbf{U}^P}{\partial t^2} = \alpha^2\ \nabla(\nabla \cdot \mathbf{U})$ $\frac{\partial^2 \mathbf{U}^S}{\partial t^2} = -\beta^2\ \nabla \times (\nabla \times \mathbf{U})$	The 3rd or 4th imaging conditions	Ma et al., 2003; Du et al., 2017;	$\mathbf{U}^P$ and $\mathbf{U}^S$ are the vector wavefields with preserving the original amplitude and phase information.
7	$\frac{\partial \tau^P}{\partial t} = (\lambda + 2\mu)\left(\frac{\partial V_x}{\partial x} + \frac{\partial V_y}{\partial y} + \frac{\partial V_z}{\partial z} \right)$ $\frac{\partial \mathbf{V}^P}{\partial t} = \frac{1}{\rho} \nabla \tau^P$ $\mathbf{V}^S = \mathbf{V} - \mathbf{V}^P$	$I^{PP} = I^{\tau} = \int \tau^P_{src}\ \tau^P_{rec}\ dt$ $I^{PS} = \int \text{sgn}^{PS}\ \left\lvert \mathbf{V}^P_{src} \right\rvert\ \left\lvert \mathbf{V}^S_{rec} \right\rvert\ dt$	Xiao and Leaney, 2010; Wang et al., 2015; Du et al., 2017; Zhang et al., 2020	$\mathbf{V}^P$ and $\mathbf{V}^S$ are the vector particle-velocity wavefields with preserving the original amplitude and phase information. τ^P is the auxiliary P-wave stress wavefields.
8	$\begin{cases} \frac{\partial V_i^P}{\partial t} = \frac{\lambda + 2\mu}{\rho(2\lambda + 2\mu)} \tau_{kk,i} \\ \frac{\partial V_i^S}{\partial t} = \frac{1}{\rho}\left(\tau_{ij,j} - \frac{\lambda + 2\mu}{2\lambda + 2\mu} \tau_{kk,i} \right) \\ \bar{v}_P = \frac{\alpha}{2(\lambda + \mu)}(\tau_{xx} + \tau_{zz}) \end{cases}$ (2D) $\begin{cases} \frac{\partial V_i^P}{\partial t} = \frac{\lambda + 2\mu}{\rho(3\lambda + 2\mu)} \tau_{kk,i} \\ \frac{\partial V_i^S}{\partial t} = \frac{1}{\rho}\left(\tau_{ij,j} - \frac{\lambda + 2\mu}{3\lambda + 2\mu} \tau_{kk,i} \right) \\ \bar{v}_P = \frac{\alpha}{(3\lambda + 2\mu)}(\tau_{xx} + \tau_{yy} + \tau_{zz}) \end{cases}$ (3D)	$I^{PP} = \int \bar{v}_{P\,\text{src}}\ \bar{v}_{P\,rec}\ dt$ $I^{PS} = \int \text{sgn}^{PS}\ \left\lvert \mathbf{V}^P_{src} \right\rvert\ \left\lvert \mathbf{V}^S_{rec} \right\rvert\ dt$	Zhou et al., 2019	$\mathbf{V}^P$ and $\mathbf{V}^S$ are firstly obtained by solving the decoupled velocity-stress equation in Zhang et al. (2007) for 2D case and Gu et al. (2015) or Zhou et al. (2016) for 3D case. $\bar{v}_P$ is the scalar P-wave particle velocity wavefield.

where $\mathbf{S}^{cor} = (S_x^{cor}\ S_y^{cor}\ S_y^{cor})^T$. Equation (9) can be expressed by

$$\begin{cases} \dfrac{\partial U_x^P}{\partial t} = \alpha \dfrac{\partial P^{cor}}{\partial x} \\ \dfrac{\partial U_y^P}{\partial t} = \alpha \dfrac{\partial P^{cor}}{\partial y} \\ \dfrac{\partial U_z^P}{\partial t} = \alpha \dfrac{\partial P^{cor}}{\partial z} \end{cases}$$

$$\begin{cases} \dfrac{\partial U_x^S}{\partial t} = -\beta\left(\dfrac{\partial S_z^{cor}}{\partial y} - \dfrac{\partial S_y^{cor}}{\partial z}\right) \\ \dfrac{\partial U_y^S}{\partial t} = -\beta\left(\dfrac{\partial S_x^{cor}}{\partial z} - \dfrac{\partial S_z^{cor}}{\partial x}\right) \\ \dfrac{\partial U_z^S}{\partial t} = -\beta\left(\dfrac{\partial S_y^{cor}}{\partial x} - \dfrac{\partial S_x^{cor}}{\partial y}\right). \end{cases} \tag{B2}$$

Based on the second-order displacement elastic-wave equation, we use the regular-grid FD operator with second-order accuracy in time and (2m)th-order accuracy in space to approximate the temporal and spatial derivatives. FD schemes for (B1) are

$$P^{cor}\big|_{i,j,k}^{n+1} = P^{cor}\big|_{i,j,k}^{n-1} - 2\Delta t\alpha\left[\mathrm{D}_x U_x + \mathrm{D}_y U_y + \mathrm{D}_z U_z\right]_{i,j,k}^{n}$$

$$\begin{cases} S_x^{cor}\big|_{i,j,k}^{n+1} = S_x^{cor}\big|_{i,j,k}^{n-1} - 2\Delta t\beta\left[\mathrm{D}_y U_z - \mathrm{D}_z U_y\right]_{i,j,k}^{n} \\ S_y^{cor}\big|_{i,j,k}^{n+1} = S_y^{cor}\big|_{i,j,k}^{n-1} - 2\Delta t\beta\left[\mathrm{D}_z U_x - \mathrm{D}_x U_z\right]_{i,j,k}^{n} \\ S_z^{cor}\big|_{i,j,k}^{n+1} = S_z^{cor}\big|_{i,j,k}^{n-1} - 2\Delta t\beta\left[\mathrm{D}_x U_y - \mathrm{D}_y U_x\right]_{i,j,k}^{n}. \end{cases} \tag{B3}$$

FD schemes for (B2) are

$$\begin{cases} U_x^P\big|_{i,j,k}^{n+1} = U_x^P\big|_{i,j,k}^{n-1} + 2\alpha\Delta t\left[\mathrm{D}_x P^{cor}\right]_{i,j,k}^{n} \\ U_y^P\big|_{i,j,k}^{n+1} = U_y^P\big|_{i,j,k}^{n-1} + 2\alpha\Delta t\left[\mathrm{D}_y P^{cor}\right]_{i,j,k}^{n} \\ U_z^P\big|_{i,j,k}^{n+1} = U_z^P\big|_{i,j,k}^{n-1} + 2\alpha\Delta t\left[\mathrm{D}_z P^{cor}\right]_{i,j,k}^{n} \\ U_x^S\big|_{i,j,k}^{n+1} = U_x^S\big|_{i,j,k}^{n-1} - 2\beta\Delta t\left[\mathrm{D}_y S_z^{cor} - \mathrm{D}_z S_y^{cor}\right]_{i,j,k}^{n} \\ U_y^S\big|_{i,j,k}^{n+1} = U_y^S\big|_{i,j,k}^{n-1} - 2\beta\Delta t\left[\mathrm{D}_z S_x^{cor} - \mathrm{D}_x S_z^{cor}\right]_{i,j,k}^{n} \\ U_z^S\big|_{i,j,k}^{n+1} = U_z^S\big|_{i,j,k}^{n-1} - 2\beta\Delta t\left[\mathrm{D}_x S_y^{cor} - \mathrm{D}_y S_x^{cor}\right]_{i,j,k}^{n} \end{cases} \tag{B4}$$

where *i, j,* and *k* denote the grid points in the *x*-, *y*-, and *z*-directions, respectively, *n* is the time index, and D_x, D_y, and D_z denote the spatial FD operators along three directions, Δt is the temporal interval.

Based on the staggered-grid FD scheme and the first-order particle-velocity elastic-wave equation [39], [40], [41], we replace the displacement U with particle-velocity V, and the staggered-grid FD schemes for (B1) are as in (B5), shown at the bottom of the page.

The staggered-grid FD schemes for (B2) are as in (B6), shown at the bottom of the page, where the subscripts containing 1/2 denote the half gridpoint in the corresponding axis. For spatial partial derivatives, an arbitrary even-order staggered-grid FD scheme can be used to approximate the operator D. Fig. 14 shows the locations of individual variables in the staggered grid. P^{cor} is located at the same node with σ_{xx}, σ_{yy}, and σ_{zz}. S_x^{cor}, S_y^{cor}, and S_z^{cor} share the same nodes with σ_{yz}, σ_{xz}, and σ_{xy}, respectively. There is no location confliction when conducting spatial FD operations, and therefore, no averaging is required.

$$P^{cor}\big|_{i,j,k}^{n+1/2} = P^{cor}\big|_{i,j,k}^{n-1/2} - \Delta t\alpha\left[\mathrm{D}_x V_x + \mathrm{D}_y V_y + \mathrm{D}_z V_z\right]_{i,j,k}^{n}$$

$$\begin{cases} S_x^{cor}\big|_{i,j+1/2,k+1/2}^{n+1/2} = S_x^{cor}\big|_{i,j+1/2,k+1/2}^{n-1/2} - \Delta t\beta\left[\mathrm{D}_y V_z - \mathrm{D}_z V_y\right]_{i,j+1/2,k+1/2}^{n} \\ S_y^{cor}\big|_{i+1/2,j,k+1/2}^{n+1/2} = S_y^{cor}\big|_{i+1/2,j,k+1/2}^{n-1/2} - \Delta t\beta\left[\mathrm{D}_z V_x - \mathrm{D}_x V_z\right]_{i+1/2,j,k+1/2}^{n} \\ S_z^{cor}\big|_{i+1/2,j+1/2,k}^{n+1/2} = S_z^{cor}\big|_{i+1/2,j+1/2,k}^{n-1/2} - \Delta t\beta\left[\mathrm{D}_x V_y - \mathrm{D}_y V_x\right]_{i+1/2,j+1/2,k}^{n} \end{cases} \tag{B5}$$

$$\begin{cases} V_x^P\big|_{i+1/2,j,k}^{n} = V_x^P\big|_{i+1/2,j,k}^{n-1} + \alpha\Delta t\left[\mathrm{D}_x P^{cor}\right]_{i+1/2,j,k}^{n-1/2} \\ V_y^P\big|_{i,j+1/2,k}^{n} = V_y^P\big|_{i,j+1/2,k}^{n-1} + \alpha\Delta t\left[\mathrm{D}_y P^{cor}\right]_{i,j+1/2,k}^{n-1/2} \\ V_z^P\big|_{i,j,k+1/2}^{n} = V_z^P\big|_{i,j,k+1/2}^{n-1} + \alpha\Delta t\left[\mathrm{D}_z P^{cor}\right]_{i,j,k+1/2}^{n-1/2} \\ V_x^S\big|_{i+1/2,j,k}^{n} = V_x^S\big|_{i+1/2,j,k}^{n-1} - \beta\Delta t\left[\mathrm{D}_y S_z^{cor} - \mathrm{D}_z S_y^{cor}\right]_{i+1/2,j,k}^{n-1/2} \\ V_y^S\big|_{i,j+1/2,k}^{n} = V_y^S\big|_{i,j+1/2,k}^{n-1} - \beta\Delta t\left[\mathrm{D}_z S_x^{cor} - \mathrm{D}_x S_z^{cor}\right]_{i,j+1/2,k}^{n-1/2} \\ V_z^S\big|_{i,j,k+1/2}^{n} = V_z^S\big|_{i,j,k+1/2}^{n-1} - \beta\Delta t\left[\mathrm{D}_x S_y^{cor} - \mathrm{D}_y S_x^{cor}\right]_{i,j,k+1/2}^{n-1/2} \end{cases} \tag{B6}$$

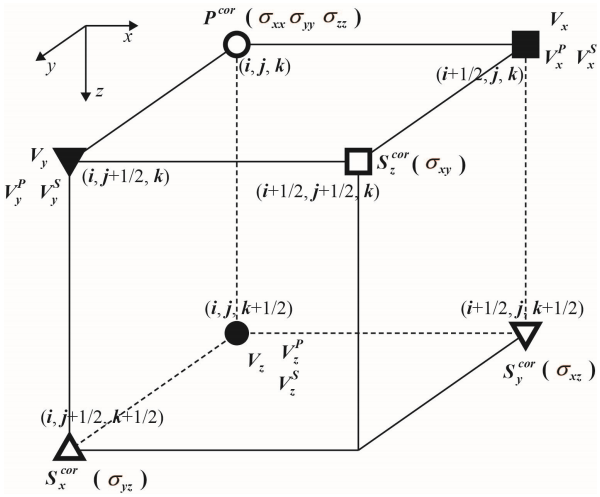

Fig. 14. Grid layout of staggered-grid FD scheme for P- and S-wave decomposition in 3-D medium.

C. FD Schemes for P and S Wave Decomposition in 2-D Medium

Here we present the regular- and staggered-grid FD schemes for P and S wave decomposition in a 2-D medium. This can be regarded as the special cases of the 3-D case in Appendix B. Under this circumstance, S^{cor} has only one component. For simplicity, the FD operator with second-order accuracy in both time and space is used. Equations (6) and (9) are expanded as follows:

$$\frac{\partial P^{cor}}{\partial t} = \alpha\left(\frac{\partial U_x}{\partial x} + \frac{\partial U_z}{\partial z}\right) \tag{C1}$$

$$\frac{\partial S^{cor}}{\partial t} = \beta\left(\frac{\partial U_x}{\partial z} - \frac{\partial U_z}{\partial x}\right)$$

$$\begin{cases} \dfrac{\partial U_x^P}{\partial t} = \alpha\dfrac{\partial P^{cor}}{\partial x} \\ \dfrac{\partial U_z^P}{\partial t} = \alpha\dfrac{\partial P^{cor}}{\partial z} \end{cases}$$

$$\begin{cases} \dfrac{\partial U_x^S}{\partial t} = \beta\dfrac{\partial S^{cor}}{\partial z} \\ \dfrac{\partial U_z^S}{\partial t} = -\beta\dfrac{\partial S^{cor}}{\partial x}. \end{cases} \tag{C2}$$

Using the regular-grid FD scheme to solve the second-order displacement elastic-wave equation, the following FD schemes are used as in (C3) and (C4), shown at the bottom of the page, where Δx is the grid interval.

If the staggered-grid FD scheme is used to solve the first-order particle-velocity elastic-wave equation, the following FD schemes are used as in (C5) and (C6), shown at the bottom of the page.

$$P^{cor}\big|_{i,j}^{n+1} = P^{cor}\big|_{i,j}^{n-1} - \alpha\frac{\Delta t}{\Delta x}\left(U_x\big|_{i+1,j}^{n} - U_x\big|_{i-1,j}^{n} + U_z\big|_{i,j+1}^{n} - U_z\big|_{i,j-1}^{n}\right)$$

$$S^{cor}\big|_{i,j}^{n+1} = S^{cor}\big|_{i,j}^{n-1} - \beta\frac{\Delta t}{\Delta x}\left(U_x\big|_{i,j+1}^{n} - U_x\big|_{i,j-1}^{n} - U_z\big|_{i+1,j}^{n} + U_z\big|_{i-1,j}^{n}\right) \tag{C3}$$

$$\begin{cases} U_x^P\big|_{i,j}^{n+1} = U_x^P\big|_{i,j}^{n-1} + \alpha\dfrac{\Delta t}{\Delta x}\left(P^{cor}\big|_{i+1,j}^{n} - P^{cor}\big|_{i-1,j}^{n}\right) \\ U_z^P\big|_{i,j}^{n+1} = U_z^P\big|_{i,j}^{n-1} + \alpha\dfrac{\Delta t}{\Delta x}\left(P^{cor}\big|_{i,j+1}^{n} - P^{cor}\big|_{i,j-1}^{n}\right) \end{cases}$$

$$\begin{cases} U_x^S\big|_{i,j}^{n+1} = U_x^S\big|_{i,j}^{n-1} + \beta\dfrac{\Delta t}{\Delta x}\left(S^{cor}\big|_{i,j+1}^{n} - S^{cor}\big|_{i,j-1}^{n}\right) \\ U_z^S\big|_{i,j}^{n+1} = U_z^S\big|_{i,j}^{n-1} - \beta\dfrac{\Delta t}{\Delta x}\left(S^{cor}\big|_{i+1,j}^{n} - S^{cor}\big|_{i-1,j}^{n}\right) \end{cases} \tag{C4}$$

$$P^{cor}\big|_{i,j}^{n+1/2} = P^{cor}\big|_{i,j}^{n-1/2} - \alpha\frac{\Delta t}{\Delta x}\left(V_x\big|_{i+1/2,j}^{n} - V_x\big|_{i-1/2,j}^{n} + V_z\big|_{i,j+1/2}^{n} - V_z\big|_{i,j-1/2}^{n}\right)$$

$$S^{cor}\big|_{i+1/2,j+1/2}^{n+1/2} = S^{cor}\big|_{i+1/2,j+1/2}^{n-1/2} - \beta\frac{\Delta t}{\Delta x}\left(V_x\big|_{i+1/2,j+1}^{n} - V_x\big|_{i+1/2,j}^{n} - V_z\big|_{i+1,j+1/2}^{n} + V_z\big|_{i,j+1/2}^{n}\right) \tag{C5}$$

$$\begin{cases} V_x^P\big|_{i+1/2,j}^{n} = V_x^P\big|_{i+1/2,j}^{n-1} + \alpha\dfrac{\Delta t}{\Delta x}\left(P^{cor}\big|_{i+1,j}^{n-1/2} - P^{cor}\big|_{i,j}^{n-1/2}\right) \\ V_z^P\big|_{i,j+1/2}^{n} = V_z^P\big|_{i,j+1/2}^{n-1} + \alpha\dfrac{\Delta t}{\Delta x}\left(P^{cor}\big|_{i,j+1}^{n-1/2} - P^{cor}\big|_{i,j}^{n-1/2}\right) \end{cases}$$

$$\begin{cases} V_x^S\big|_{i+1/2,j}^{n} = V_x^S\big|_{i+1/2,j}^{n-1} + \beta\dfrac{\Delta t}{\Delta x}\left(S^{cor}\big|_{i+1/2,j+1/2}^{n-1/2} - S^{cor}\big|_{i+1/2,j-1/2}^{n-1/2}\right) \\ V_z^S\big|_{i,j+1/2}^{n} = V_z^S\big|_{i,j+1/2}^{n-1} - \beta\dfrac{\Delta t}{\Delta x}\left(S^{cor}\big|_{i+1/2,j+1/2}^{n-1/2} - S^{cor}\big|_{i-1/2,j+1/2}^{n-1/2}\right) \end{cases} \tag{C6}$$

REFERENCES

[1] W.-F. Chang and G. A. McMechan, "Elastic reverse-time migration," *Geophysics*, vol. 52, no. 10, pp. 1365–1375, 1987.

[2] R. Sun and G. A. McMechan, "Scalar reverse-time depth migration of prestack elastic seismic data," *Geophysics*, vol. 66, no. 5, pp. 1519–1527, 2001.

[3] R. Sun, G. A. Mcmechan, C.-S. Lee, J. Chow, and C.-H. Chen, "Prestack scalar reverse-time depth migration of 3D elastic seismic data," *Geophysics*, vol. 71, no. 5, pp. S199–S207, Sep. 2006.

[4] S. Chattopadhyay and G. A. Mcmechan, "Imaging conditions for prestack reverse-time migration," *Geophysics*, vol. 73, no. 3, pp. S81–S89, May 2008.

[5] W. Zhang and Y. Shi, "Imaging conditions for elastic reverse time migration," *Geophysics*, vol. 84, no. 2, pp. S95–S111, 2019.

[6] J. Yan and P. Sava, "Isotropic angle-domain elastic reverse-time migration," *Geophysics*, vol. 73, no. 6, pp. S229–S239, Nov. 2008.

[7] Y. Duan and P. Sava, "Scalar imaging condition for elastic reverse time migration," *Geophysics*, vol. 80, no. 4, pp. S127–S136, Jul. 2015.

[8] K. Aki and P. G. Richards, *Quantative Seismology: Theory and Methods*. San Francisco, CA, USA: Acoustical Society of America, 1980.

[9] J. Dellinger and J. Etgen, "Wave-field separation in two-dimensional anisotropic media," *Geophysics*, vol. 55, no. 7, pp. 914–919, Jul. 1990.

[10] R. Sun, G. A. Mcmechan, H. Hsiao, and J. Chow, "Separating P- and S-waves in prestack 3D elastic seismograms using divergence and curl," *Geophysics*, vol. 69, no. 1, pp. 286–297, Jan. 2004.

[11] Q. Du, X. Gong, M. Zhang, Y. Zhu, and G. Fang, "3D PS-wave imaging with elastic reverse-time migration," *Geophysics*, vol. 79, no. 5, pp. S173–S184, Sep. 2014.

[12] Q. Zhang and G. A. Mcmechan, "2D and 3D elastic wavefield vector decomposition in the wavenumber domain for VTI media," *Geophysics*, vol. 75, no. 3, pp. D13–D26, May 2010.

[13] Z. Li, P. Yong, J. Huang, Q. Li, and B. Gu, "Elastic wave reverse time migration based on vector wavefield seperation," *J. China Univ. Petroleum*, vol. 40, no. 1, pp. 42–48, 2016.

[14] J. Yang, H. Zhu, W. Wang, Y. Zhao, and H. Zhang, "Isotropic elastic reverse time migration using the phase- and amplitude-corrected vector P- and S-wavefields," *Geophysics*, vol. 83, no. 6, pp. S489–S503, Nov. 2018.

[15] W. Wang, G. A. Mcmechan, and Q. Zhang, "Comparison of two algorithms for isotropic elastic P and S vector decomposition," *Geophysics*, vol. 80, no. 4, pp. T147–T160, Jul. 2015.

[16] R. Sun, J. Chow, and K.-J. Chen, "Phase correction in separating P- and S-waves in elastic data," *Geophysics*, vol. 66, no. 5, pp. 1515–1518, 2001.

[17] R. Sun, G. A. Mcmechan, and H.-H. Chuang, "Amplitude balancing in separating P- and S-waves in 2D and 3D elastic seismic data," *Geophysics*, vol. 76, no. 3, pp. S103–S113, May 2011.

[18] H. Zhu, "Elastic wavefield separation based on the Helmholtz decomposition," *Geophysics*, vol. 82, no. 2, pp. S173–S183, Mar. 2017.

[19] D. Ma and G. Zhu, "Numerical modeling of P-wave and S-wave separation in elastic wavefield," *Oil Geophy. Propsecting*, vol. 38, no. 5, pp. 482–486, 2003.

[20] Z. Li, H. Zhang, Q. Liu, and W. Han, "Numeric simulation of elastic wavefield separation by staggering grid high-order finite-difference algorithm," *Oil Geophy. Propsecting*, vol. 42, no. 5, p. 510, 2007.

[21] Z. Jianlei, T. Zhenping, and W. Chengxiang, "P- and S-wave-separated elastic wave-equation numerical modeling using 2D staggered grid," in *Proc. SEG Tech. Program Expanded Abstr.*, Jan. 2007, pp. 2104–2109.

[22] X. Xiao and W. S. Leaney, "Local vertical seismic profiling (VSP) elastic reverse-time migration and migration resolution: Salt-flank imaging with transmitted P-to-S waves," *Geophysics*, vol. 75, no. 2, pp. S35–S49, Mar. 2010.

[23] C. Tang and G. A. McMechan, "Multidirectional-vector-based elastic reverse time migration and angle-domain common-image gathers with approximate wavefield decomposition of P- and S-waves," *Geophysics*, vol. 83, no. 1, pp. S57–S79, 2018.

[24] A. H. Shabelansky, A. E. Malcolm, M. C. Fehler, X. Shang, and W. L. Rodi, "Source-independent full wavefield converted-phase elastic migration velocity analysis," *Geophys. J. Int.*, vol. 200, no. 2, pp. 954–968, Feb. 2015.

[25] B. Gu, Z. Li, P. Yang, W. Xu, and J. Han, "Elastic least-squares reverse time migration with hybrid l_1/l_2 misfit function," *Geophysics*, vol. 82, no. 3, pp. S271–S291, May 2017.

[26] X. Zhou, X. Chang, Y. Wang, and Z. Yao, "Amplitude-preserving scalar PP and PS imaging condition for elastic reverse time migration based on a wavefield decoupling method," *Geophysics*, vol. 84, no. 3, pp. S113–S125, May 2019.

[27] T. Hu, H. Liu, X. Guo, Y. Yuan, and Z. Wang, "Analysis of direction-decomposed and vector-based elastic reverse time migration using the Hilbert transform," *Geophysics*, vol. 84, no. 6, pp. S599–S617, Nov. 2019.

[28] W. Zhang, J. Gao, Z. Gao, and Y. Shi, "2D and 3D amplitude-preserving elastic reverse time migration based on the vector-decomposed P- and S-wave records," *Geophys. Prospecting*, vol. 68, no. 9, pp. 2712–2737, Nov. 2020.

[29] Z. Li, Y. Liu, G. Liang, G. Xue, and R. Wang, "First-order particle velocity equations of decoupled P- and S-wavefields and their application in elastic reverse time migration," *Geophysics*, vol. 86, no. 6, pp. S387–S404, Nov. 2021.

[30] A. Balch and C. Erdemir, "Sign-change correction for prestack migration of P-S converted wave reflections," *Geophys. Prospecting*, vol. 42, no. 6, pp. 637–663, 1994.

[31] X.-B. Xie and R.-S. Wu, "Multicomponent prestack depth migration using the elastic screen method," *Geophysics*, vol. 70, no. 1, pp. S30–S37, Jan. 2005.

[32] Q. Du, Y. Zhu, and J. Ba, "Polarity reversal correction for elastic reverse time migration," *Geophysics*, vol. 77, no. 2, pp. S31–S41, Mar. 2012.

[33] R. Yan and X.-B. Xie, "An angle-domain imaging condition for elastic reverse time migration and its application to angle gather extraction," *Geophysics*, vol. 77, no. 5, pp. S105–S115, Sep. 2012.

[34] Z. Li, X. Ma, C. Fu, and G. Liang, "Wavefield separation and polarity reversal correction in elastic reverse time migration," *J. Appl. Geophys.*, vol. 127, pp. 56–67, Apr. 2016.

[35] C. Wang, J. Cheng, and B. Arntsen, "Scalar and vector imaging based on wave mode decoupling for elastic reverse time migration in isotropic and transversely isotropic media," *Geophysics*, vol. 81, no. 5, pp. S383–S398, Sep. 2016.

[36] Q. Du, C. Guo, Q. Zhao, X. Gong, C. Wang, and X.-Y. Li, "Vector-based elastic reverse time migration based on scalar imaging condition," *Geophysics*, vol. 82, no. 2, pp. S111–S127, Mar. 2017.

[37] Y.-S. Liu, S.-L. Liu, M.-G. Zhang, and D.-T. Ma, "An improved perfectly matched layer absorbing boundary condition for second order elastic wave equation," *Prog. Geophys.*, vol. 27, no. 5, pp. 2113–2122, 2012.

[38] G. S. Martin, K. J. Marfurt, and S. Larsen, "Marmousi-2: An updated model for the investigation of AVO in structurally complex areas," in *Proc. SEG Tech. Program Expanded Abstr.*, Jan. 2002, pp. 1979–1982.

[39] J. Virieux, "SH-wave propagation in heterogeneous media: Velocity-stress finite-difference method," *Geophysics*, vol. 49, no. 11, pp. 1933–1942, 1984.

[40] J. Virieux, "P-SV wave propagation in heterogeneous media: Velocity-stress finite-difference method," *Geophysics*, vol. 51, no. 4, pp. 889–901, Apr. 1986.

[41] R. W. Graves, "Simulating seismic wave propagation in 3D elastic media using staggered-grid finite differences," *Bull Seismol. Soc. Amer.*, vol. 86, no. 4, pp. 1091–1106, Aug. 1996.

Na Fan received the B.S. degree in geophysics from Wuhan University, Wuhan, China, in 2010, and the Ph.D. degree from the Institute of Geology and Geophysics, Chinese Academy of Science, Beijing, China, in 2015.

She is currently an Associate Professor at the Yangtze University, Wuhan. Her research interests include seismic data processing, forward modeling, inversion, imaging, and seismic nuclear monitoring.

Xiao-Bi Xie received the B.S. degree in physics from the University of Sciences and Technology of China, Hefei, China, in 1977, and the M.S. and Ph.D. degrees in geophysics from the Institute of Geophysics, Chinese Academy of Sciences, Beijing, China, in 1981 and 1988, respectively.

He is currently a Researcher at the Institute of Geophysics and Planetary Physics, University of California, Santa Cruz, CA, USA. His research covers two areas. In applied seismology, he focuses on developing novel methods for seismic modeling, imaging, and velocity inversion. In earthquake seismology, he is investigating regional seismic wave excitation and propagation with numerical simulations and real data analysis.

Lian-Feng Zhao received the B.S. degree from the Eastern China Institute of Technology, Fuzhou, China, in 1993, and the M.S. and Ph.D. degrees from the Chengdu University of Technology, Chengdu, China, in 2000 and 2003, respectively, all in geophysics.

He is currently a Professor at the Institute of Geology and Geophysics, Chinese Academy of Sciences, Beijing, China. His research interests include seismic source mechanisms, wave propagation, seismic tomography, nuclear monitoring, and deep structure and dynamic process.

Xiyan Zhou received the B.S. degree from the Chengdu University of Technology, Chengdu, China, in 2014, and the Ph.D. degree from the Institute of Geology and Geophysics, Chinese Academy of Sciences, Beijing, China, in 2019, both in geophysics.

He is currently a Lecturer at the Chengdu University of Technology, Chengdu. His research interests include seismic data processing, elastic wavefield separation, and reverse time migration.

Zhen-Xing Yao received the B.S. degree in physics from Beijing University, Beijing, China, in 1962, and the M.S. degree in geophysics from the Institute of Geophysics, Chinese Academy of Sciences, Beijing, in 1966.

He is currently a Professor at the Institute of Geology and Geophysics, Chinese Academy of Sciences. His research interests include seismic source mechanisms, wave propagation, synthetic seismogram, nonlinear inversion, hydraulic fracturing, seismic nuclear monitoring, and deep structure and dynamic process.